STIFF MICROSCALE FORCING AND SOLITARY WAVE REFOCUSING*

JUAN CARLOS MUÑOZ GRAJALES† AND ANDRÉ NACHBIN‡

Abstract. This study is focused on wave propagation in heterogeneous media and on capturing the cumulative effect due to small-scale orographic features. More specifically on designing a numerical method capable of capturing these effects over long propagation distances (the *macroscale*) when a weakly dispersive, weakly nonlinear solitary wave (the *mesoscale*) is forced by a disordered *microscale*. An accurate and stable numerical scheme is presented for solving a variable coefficient nonlinear Boussinesq system, in the presence of highly oscillatory solutions, together with a new result on its linear stability analysis. The stability analysis focuses on describing the stiffness promoted by the topography's microscale and how it can be removed through an appropriate change of coordinates. The new mathematical formulation acts as a preconditioning at the differential equation level and the spectrum's range becomes insensitive to the microscale. The other goal of this paper is to present the time-reversal and refocusing for solitary waves. In previous works the effects of dispersion and of nonlinearity have been analysed separately. The time-reversed refocusing of solitary waves is observed numerically over a set of different simulations. Presently there is no mathematical theory for the time-reversed refocusing of solitons. Hopefully these simulations will shed some light in this direction.

Key words. solitary waves, inhomogeneous media, refocusing

AMS subject classifications. 76B07, 76B15, 35Q

1. Introduction. Wave–topography interaction has been the subject of considerable mathematical research. The physical applications range from coastal surface waves [28] to atmospheric flows over mountain ranges [3, 15]. In particular, the interaction of waves with fine features of the topography is of great interest. As pointed out in the introduction to the *Orography* proceedings [15] of the European Centre for Medium-Range Weather Forecasts (ECMWF), the "representation (...) of subgrid-scale orographic processes is recognized as crucial to numerical weather prediction at all time ranges". In the atmospheric literature *orography* implies mountain ranges [3].

Our study is focused on capturing the effect of small-scale orographic features, which we refer to as the *microscale*. More specifically on designing an accurate and stable numerical method capable of capturing the cumulative effects over long propagation distances when a pulse shaped wave is forced on a disordered microscale. The application is coastal gravity waves propagating from deep to shallow waters. They are transformed due to shoaling, refraction, diffraction and reflection. In order to concentrate on the main scattering mechanism connected with the time-reversed refocusing phenomenon, to be described below, we consider the normal incidence of surface pulse shaped waves. These waves propagate over topographies containing a smooth slowly varying profile together with disordered small-scale features. As pointed out, our goal is to capture the wave-microstructure interaction. Time-reversal can be viewed as a tool by which the waveform inversion is performed, when a good numerical model is available [37]. Through the time-reversal simulation with the transmitted (or reflected) signal the initial ocean disturbance can be reconstructed. In this paper a

*This work was supported by CNPq/Brazil under Grant 300368/96-8.

†Instituto de Matemática Pura e Aplicada, Est. D. Castorina 110, Jardim Botânico, Rio de Janeiro, RJ 22460-320, Brazil (juanc@impa.br). Current address: Department of Mathematics, Universidad del Valle, Cali, Colombia.

‡Instituto de Matemática Pura e Aplicada, Est. D. Castorina 110, Jardim Botânico, Rio de Janeiro, RJ 22460-320, Brazil (nachbin@impa.br).

numerical method is analysed and used for the (multiple scale) simulation of solitary waves in the presence of a rapidly varying disordered topography.

We consider gravity driven long water waves, propagating in one-dimensional channels in the regime where the fluid is considered to be inviscid and incompressible. The microscale comes from the irregular topography at the bottom of the shallow channel. Note that the *long wave/shallow water* regime is dictated by having a small depth to wavelength ratio. Velocity and wave elevation at the free surface are described through a terrain-following Boussinesq system [31] which contain a Burgers' type nonlinearity controlled by the wave amplitude. The Boussinesq system is weakly dispersive, weakly nonlinear.

First we show how the microscale of the orography makes the standard Boussinesq system become stiff. Namely as we gradually decrease the length scale of orography we get a wider spectrum range for a corresponding frequency dependent system of ordinary differential equations. The spectrum scales like the reciprocal of the microscale. We then show how this problem can be numerically preconditioned by reformulating the partial differential equations in a new coordinate system which removes the spectrum range's sensitivity to the microscale. Hence an efficient and stable numerical code is developed for solving the nonlinear dispersive equations in the presence of highly oscillatory solutions. It provides an accurate tool to conduct numerical experiments on the time-reversed refocusing of solitary waves. These experiments are performed over large time intervals. Several weakly dispersive and weakly nonlinear experiments were validated in [30]. In the present work we describe in detail properties of the numerical scheme. This scheme was adapted from the work of Wei and Kirby [45] where the standard (slowly varying) Boussinesq system was considered. In particular we show how the stiffness promoted by the topography's microscale can be removed using the new mathematical formulation given in [31]. This is typically a problem of multiple scales. We have a long wave (the *mesoscale*) propagating over an orography containing fine features (the *microscale*). The phenomena of interest are observed only at large propagation distances (the *macroscale*) so that the pulse can interact with the orography's microscale long enough in order to exhibit nontrivial (cumulative) properties. We then proceed to performing time-reversal experiments, in particular with solitary waves.

A time-reversal mirror is, roughly speaking, a device which is capable of receiving an acoustic signal in time, keeping it in memory and sending it back into the medium in the reversed direction of time. In the context of ultrasounds time-reversal mirrors have been developed and their effect studied experimentally by Mathias Fink and his collaborators at the Laboratoire Ondes et Acoustique (ESPCI-Paris). Many articles reporting experiments and theoretical results can be found through the laboratory's website. The main effect is the refocusing of the scattered signal after time-reversal in a random medium: an acoustic pulse is sent in a disordered medium generating a "noisy" scattered signal which is time-reversed and sent back into the medium. The new scattered signal is a pure pulse with a shape similar to the initial pulse. Amazingly its "refocusing" takes place in time and space and seems to be independent of the realization of the medium. Experiments in the context of underwater acoustics have been conducted by Kuperman et al.[25] and show the same phenomenon. New developments for time-reversal in a waveguide can be found in [24]. We also refer to reference [17] for a description on Kuperman's experiments and further references.

Regarding the scaling we chose to work in the regime where the medium's correlation length is smaller than the typical wavelength of the pulse. This choice was made due to our theoretical and computational experience [30, 32, 33, 34] in this regime together with the great amount of mathematical theory available in [2, 7, 8]. Nevertheless it is well known that this is not the only regime for time-reversed refocusing to take place. Results in the high-frequency regime (where the correlation length is comparable to the carrier wavelength) can be found in [4, 5, 10, 11, 18, 44].

From the theoretical point of view, a first proof of this refocusing effect has been obtained by Clouet and Fouque [9] in the context of a one-dimensional random medium for which only the time refocusing is relevant. The refocusing is obtained by using asymptotics in the regime where, as mentioned above, there are three well separated scales:

$$\frac{\text{correlation length of the medium}}{\text{wavelength of the pulse}} \approx \frac{\text{wavelength of the pulse}}{\text{distance of propagation}} \ll 1.$$

The relative order between the microscale, mesoscale and macroscale will be measured by small dimensionless parameters. The fluctuations of the medium are not assumed to be small but rather of the order of several tens of percent. This result has been extended to the case of 3D layered media by Ndzie [35] where it is shown that refocusing takes place in time as well as in space. More recently space refocusing has been analysed in the context of small fluctuation and the parabolic approximation by Blomgren, Papanicolaou and Zhao [5] and Papanicolaou, Ryhzik and Sølna [38]. They show that time-reversal and randomness helps in "beating" the diffraction limit: they call this effect super-resolution. A complete proof of super-resolution for three-dimensional randomly layered media has been obtained in Fouque and Sølna [22]. Potential applications of these effects are numerous in imaging and wireless communication.

Time-reversal experiments can be performed for the transmitted or for the reflected signal. We point out that time-reversal in reflection (TRR) [19, 43] has been much less explored than time-reversal in transmission (TRT) [4, 5, 10, 11, 16, 17, 18, 24, 25, 41, 44]. One of the goals of this paper is to present the time-reversal and refocusing for solitary waves. In previous work the effect of dispersion [20] and of nonlinearity [21] have been analysed separately. Presently there is no theory for the time-reversed refocusing of solitons. We hope that the simulations presented here can shed some light in this direction. On the other hand experimental work has been conducted by Tanter *et al.* [44] and considers the effect of nonlinearity. Time-reversibility is observed for a transmitted nonlinear sinusoidal wave in a homogeneous medium. They report that TRT happens only for propagation shorter than the shock formation distance. Recently Fouque, Garnier and Nachbin [21] have analysed time-reversal for weakly nonlinear waves. It was shown that to leading order the transmitted pulse is governed by a viscous Burgers equation, where the "apparent viscosity" is due to the stochastic microscale forcing. Therefore the viscous shock structure does not evolve torwards the singularity formation. For solitons we have the additional regularization due to dispersion.

Regarding applications in water waves, the problem of waveform inversion has been studied by adjoint methods in Pires and Miranda [37] and the references within. Their goal is to characterize the initial sea surface displacement due to tsunamigenic earthquakes. In other words one would like to recover (numerically) relevant details of a tsunami source from tidal gauge observations. In our case, instead of performing the backward numerical integration of the corresponding adjoint equations, we use the (same) forward numerical model but with the time-reversed data. Waveform inversion is obtained through the time-reversed refocusing effect. In Fouque, Garnier and Nachbin [20] the mathematical theory for the time-reversal of linear hyperbolic waves has been extended to the more realistic case of linear dispersive waves. It has also been extended to weakly nonlinear waves [21]. To the present date it has not been extended to weakly dispersive, weakly nonlinear waves.

This paper is organized as follows. First we introduce the dispersive model governing long waves propagating over a wide class of topographies. In section 3 we discuss properties of the model including the stiffness due to the microscale forcing. We show how reformulating the mathematical model in a different coordinate system can change the spectrum range for the linearized problem. In section 4 we introduce the numerical model used for the nonlinear Boussinesq equation. In section 5 we present numerical experiments illustrating pulse stabilization while in section 6 we perform scientific computing experiments in time-reversal and refocusing for solitary waves. Finally in section 7 we have the Conclusions.

2. Governing equations. The dispersive wave model we adopt in this work is the one-dimensional terrain-following Boussinesq system derived by Nachbin [31]:

$$
\begin{aligned}
&M(\xi)\eta_t + \left(\left(1+\frac{\alpha\eta}{M(\xi)}\right)u\right)_\xi = 0, \\
&u_t + \eta_\xi + \frac{\alpha}{2}\left(\frac{u^2}{M(\xi)^2}\right)_\xi - \frac{\beta}{3}u_{\xi\xi t} = 0,
\end{aligned}
\tag{2.1}
$$

where the parameter $\alpha = a_o/h_o$ regulates nonlinearity and $\beta = h_o^2/\ell_p^2$ the level of dispersion. The characteristic wave amplitude is a_o, the characteristic wavelength is ℓ_p and the typical depth is h_o. Here ξ and t are the space and time coordinates, respectively, $\eta = \eta(\xi, t)$ is the wave elevation and $u = u(\xi, t)$ is the weigthed depth-averaged terrain-following velocity [31]. The variable coefficient $M(\xi)$ is a smooth orography dependent function which appears as a consequence of a change of variables from cartesian to curvilinear coodinates [31]. The topography profile can be a multi-valued function as sketched in Figure 2.1. When the parameter β is small we are in the shallow channel/long wave regime. Equivalently this is called the weakly-dispersive regime which models waves in the coastal region.

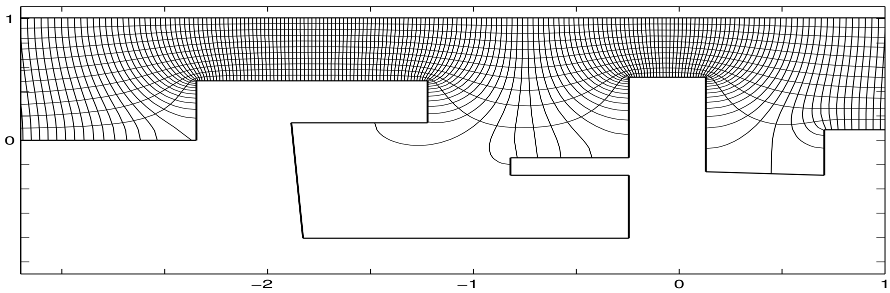

FIG. 2.1. *Curvilinear coordinate system for a multivalued topography profile.*

The pulse stabilization and refocusing phenomena we wish to study takes place in the regime where the pulse width ℓ_p is broad with respect to the correlation length of the medium fluctuations ℓ (i.e., the depth varies rapidly). This small scale is built into the coefficient $M(\xi)$ as will become clear below. Here we adopt the ratio $\gamma = \ell/\ell_p$ to be 1/10. Furthermore, the total propagation distance L_o over the irregular section of the coast considered is taken to be larger than the typical pulse width ℓ_p: $\ell_p/L_o \ll 1$.

3. Theoretical and numerical properties of the Boussinesq model. In this section we discuss important properties of model (2.1) which makes it appropriate for exploring the mechanisms of scattering and refocusing of dispersive waves in highly variable media.

As shown in [31], system (2.1) is valid as an asymptotic approximation of the potential theory equations for arbitrary orographies (even non-differentiable or rapidly varying) provided that $0 < \alpha << 1$ and $0 < \beta << 1$ (small wave amplitude and shallow depth). Furthermore the presence of both dispersive and nonlinear terms in (2.1) allows for the existence of solitary waves, i.e. pulses travelling with constant velocity without changing its shape over a constant depth. These features enable the study of solitary waves in a random environment.

Other models for weakly dispersive, weakly nonlinear systems such as Peregrine's [40]

$$\begin{aligned} &\eta_t + [(h + \alpha\eta)u]_x = 0, \\ &u_t + \eta_x + \alpha u u_x + \beta\left(\frac{h^2}{6}u_{xxt} - \frac{h}{2}\partial_x^2(hu_t)\right) = 0, \end{aligned} \tag{3.1}$$

are valid provided that the **mild slope condition**

$$m = O\left(\frac{h'(x)}{kh}\right) << 1, \tag{3.2}$$

is satisfied (c.f. Mei [28], pag. 59). Here, parameter k represents the typical wavenumber, $u = u(x,t)$ and $\eta(x,t)$ denote the averaged velocity and the wave elevation, respectively. Further $h(x) = 1 + \delta n(x/\gamma)$ is a function describing the channel's depth. Parameter γ measures the ratio inhomogeneities/wavelength, δ represents the amplitude of the bottom's irregularities and α and β are defined as for model (2.1). Implicity, it is also assumed that the derivative of the depth function is well-defined since the variable coefficients in system (3.1) contain derivatives of the function $h(x)$.

In contrast, in the terrain-following system (2.1) the physical orography $h(x)$ is replaced by the metric coefficient

$$M(\xi;\beta) = 1 + \frac{\pi}{4\sqrt{\beta}} \int_{-\infty}^{\infty} \frac{\delta\, n(x(\xi_0, -\sqrt{\beta})/\gamma)}{cosh^2 \frac{\pi}{2\sqrt{\beta}}(\xi_0 - \xi)} d\xi_0.$$

Here the function $n(x)$ describes the bottom fluctuations (see [31]). Note that the function $M(\xi;\beta)$ is smooth. Here we present explicitly the dependence of the metric coefficient on the dispersion scale β. The scale $\sqrt{\beta}$ plays a role in the smoothing effect of the coefficients of the terrain-following formulation [31]. See Figure 3.1 where we compare $h(x)$ and $M(\xi(x))$ for the case of a periodic bottom with "corners".

In dimensionless variables, condition (3.2) can be expressed as

$$m = O\left(\frac{\delta n'(x/\gamma)}{2\pi\gamma\sqrt{\beta}}\right) << 1. \tag{3.3}$$

We remark that, in this work, condition (3.3) is not satisfied because the depth's correlation length ℓ is small for a rapidly-varying orography. Furthermore, we are considering general non-differentiable orographies. The terrain-following system (2.1) extends the regime of validity of system (3.1) being applicable even for non-differentiable arbitrary orographies, which turns the mild slope condition unnecessary [31]. Its only restriction is that the dispersion and the nonlinearity parameters β, α be small which is typical for Boussinesq systems. As expected, models (3.1) and (2.1) coincide when condition (3.3) is fulfilled. This fact is corroborated through numerical simulations on both models. The numerical scheme used to solve systems (2.1) and (3.1) will be discussed in the next section.

We construct the periodic piecewise linear orography as displayed in Figure 3.1. It consists of five equal triangles with base of length 3 and height 0.5. This way the inhomogeneities cover the interval [0,15], the amplitude of the fluctuations is $\delta = 0.5$ and the correlation length is $\ell = 3.0$. With this setup note that we have a slowly-varying bottom with slope 1:3, where we will take $\beta = 0.01$ and therefore $m \approx 0.5$. Therefore we are within the range of application of both model (3.1) and (2.1).

The corresponding orography-dependent coefficient $M(x;\beta)$ is computed by using Driscoll's package [13] and is superimposed to the physical orography in Figure 3.1. Note that in this case the major difference between them is at the mountain's peaks and valleys where $M(x)$ is smooth.

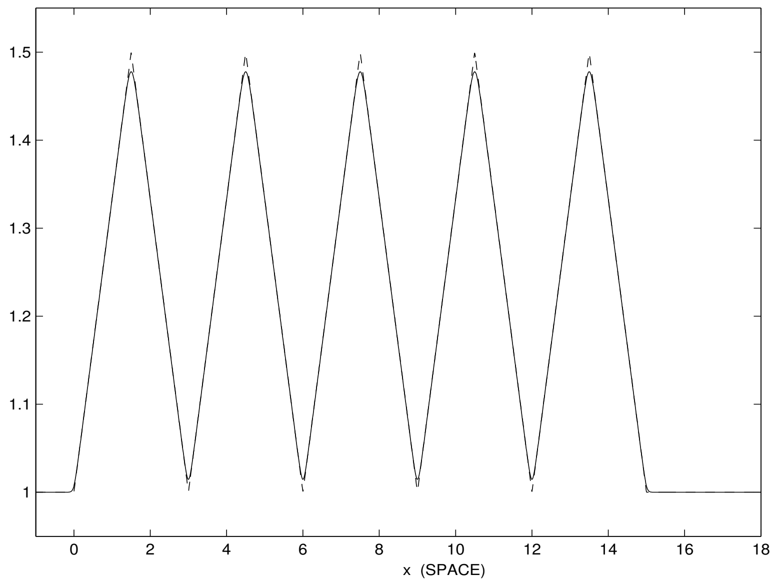

FIG. 3.1. *Free surface coefficient* $M(\xi(x);\beta = 0.01)$ *(in solid line) superimposed to a periodic piecewise linear orography* $h(x)$ *(in dashed line).*

We compute the numerical solution for systems (2.1) and (3.1) forced by functions $M(x;\beta)$ and $h(x)$, respectively. In this experiment the level of dispersion and nonlinearity are taken to be $\alpha = \beta = 0.01$. The numerical parameters for both experiments are $J = 2000$ mesh points, $N = 1500$ time steps with $\Delta\xi = 0.02$, $\Delta t = 0.01$ and the computational domain is [-20,20]. The initial disturbance is a Gaussian of effective support one located at position $x = 0$. The ratio inhomogeneities/wavelength is set to roughly 3.0.

The numerical solutions at time $t = 15$ for both models are visualized in Figure 3.2(A), each on its corresponding independent spatial variable. To establish a comparison between these solutions we replot them in Figure 3.2(B) but now on the physical spatial variable x. The change of variable $\xi \to x$ was performed by using the routine **eval** in Driscoll's package. Note that the traces are in perfect agreement showing the consistency between the two models in the slowly-varying depth regime. Nevertheless, small spurious oscillations are observed in the numerical solution of system (3.1). This can be seen (with a solid line) in the detail presented in (C). We believe that this is due to the acute corners where function $h(x)$ is non-differentiable and also the fact that the variable coefficient $h(x)$ appears in front of the dispersive term of the system. It has an impact on the solution of the linear system involved in the Boussinesq solver (see section 4). When the mesh size is refined substantially up to $J = 20000$, $N = 15000$ the spurious oscillations do not disappear completely. We also obtained similar results when the depth's slope was decreased up to 1:10.

On the other hand, in model (2.1) the coefficient of the dispersive term $u_{\xi\xi t}$ is constant and all variable coefficients are smooth. This fact strongly affects the performance of the Boussinesq solver used, in particular for multiscale problems. We corroborate this in the numerical simulation for model (2.1) displayed in Figure 3.2(B). We obtain a smooth numerical solution with a low computational cost. We point out this fact as an important numerical advantage of system (2.1). All numerical simulations were done efficiently on a PC using MATLAB. Moreover several numerical experiments in the presence of disordered rapidly topographies were performed in [29, 30] illustrating, with great accuracy, the theoretical results developed. In the next subsection we show how the microscale of the orography makes system (3.1) become stiff. Namely as we gradually decrease the length scale of orography we get a wider spectrum for a corresponding frequency dependent system of ordinary differential equations. By changing coordinate systems the eigenvlaues are automatically rescaled to a smaller interval. In other words we are preconditioning the numerical model through a change of variables in the mathematical model.

3.1. Removing the stiff microscale forcing due to the orography. In this subsection we show how the range of eigenvalues can be changed by reformulating the dispersive system of partial differential equations. Namely by going from a cartesian to a curvilinear coordinate system [31]. In some sense this strategy has already been explored successfully, as for example, by Hou, Lowengrub and Shelley [23]. Hou *et al.* used an equal arclength spacing in their mathematical formulation for the evolution of Lagrangian particles along a fluid interface. Their clever change of variables (from a nonuniform distribution to an equally spaced one) removed the problem's stiffness by eliminating high frequency components generated due to particle compression. Here we use a disordered (conformal mapping) change of variables [31]. The new coordinate system removes the stiffness promoted along the domain's boundary due the presence of the orography's microscale. Namely in the new coordinate ξ the mesh is equally spaced while the smooth metric term $M(\xi)$ incorporates the disorder, hence eliminating (by averaging) some high frequency components. Another advantage is that the variable coefficient, and its derivatives, move away from the equation's highest derivative (i.e. the third order dispersive term) and positions itself at the first order transport term.

To put the above comments in a more quantitative framework we start with the (cartesian) linear version of the dispersive model by Peregrine [40]:

$$\eta_t + [(h(x/\gamma)\ u)]_x = 0, \tag{3.4}$$

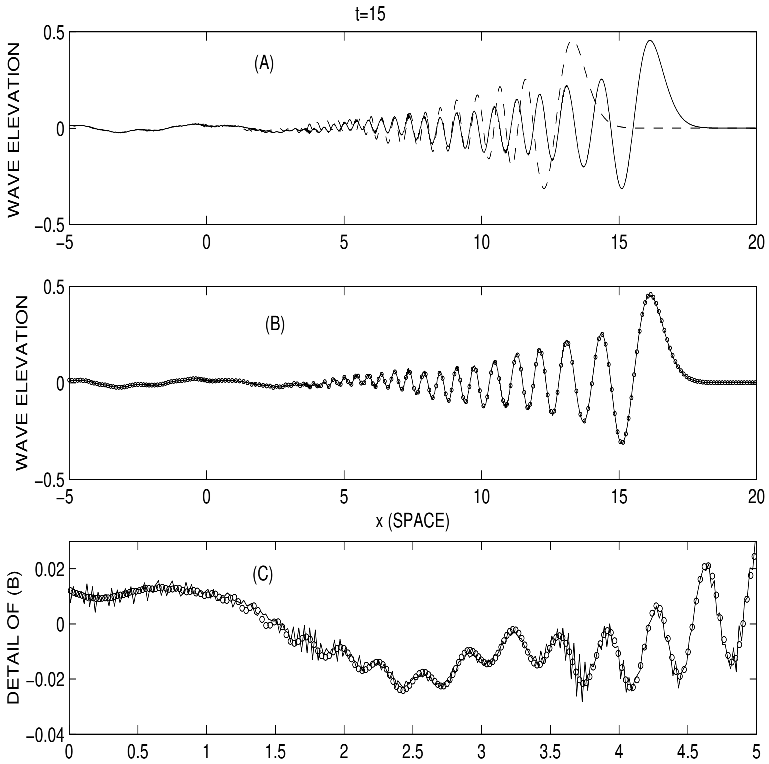

FIG. 3.2. **(A)** *Dashed line : model (2.1). Solid line : model (3.1).* **(B)** *Dotted line : model (2.1). Solid line : model (3.1). Now they are both visualized in the physical spatial variable x.* **(C)** *Detail of (B). The oscillations in solid line correspond to system (3.1) . In all experiments we set $\alpha = 0.01$, $\beta = 0.01$. The topography's correlation length is $\ell = 1.5$ and the amplitude of fluctuations is $\delta = 0.5$.*

$$u_t + \eta_x + \beta \left(\frac{h^2(x/\gamma)}{6} u_{xxt} - \frac{h(x/\gamma)}{2} \partial_x^2 (h(x/\gamma)\ u_t) \right) = 0.$$

This system is valid when

$$O\left(\frac{\delta n'(x/\gamma)}{2\pi\sqrt{\beta}} \right) << \gamma. \tag{3.5}$$

Taking a Fourier transform in time we have that

$$\begin{aligned} &(-i\omega)\hat{\eta} + (h(x/\gamma)\ \hat{u})_x = 0, \\ &(-i\omega)\hat{u} + \hat{\eta}_x = \beta \left[\frac{h(x/\gamma)}{2} \left(-i\omega h(x/\gamma)\hat{u}\right)_{xx} - \frac{h^2(x/\gamma)}{6} (-i\omega)\hat{u}_{xx} \right]. \end{aligned} \tag{3.6}$$

Using the first equation we can rewrite it as a first order system

$$\begin{aligned} &\hat{u}_x = -(\frac{h_x}{h})\ \hat{u} + (\frac{i\omega}{h})\ \hat{\eta}, \\ &\hat{\eta}_x = \frac{1}{1 - \frac{\beta}{3}\omega^2 h} \left[i\omega \left(1 - \frac{\beta}{6} h h_{xx} + \frac{\beta}{3} h_x^2 \right) \hat{u} + \left(\frac{\beta}{3}\omega^2 h_x \right) \hat{\eta} \right], \end{aligned} \tag{3.7}$$

where $h_x \equiv h'/\gamma$. The characteristic polynomial for the variable coefficient matrix is

$$p(\lambda) = \lambda^2 - \lambda \left[\frac{h_x}{h} - \frac{\frac{\beta}{3}\omega^2 h_x}{1 - \frac{\beta}{3}\omega^2 h}\right] + \frac{\omega^2}{h}\left[\frac{1 - \frac{\beta}{6}hh_{xx} + \frac{\beta}{3}h_x^2}{1 - \frac{\beta}{3}\omega^2 h}\right] = 0.$$

The eigenvalues are

$$\lambda^{\pm}(x) = -\frac{h'}{\gamma}\left(1 - \frac{1/2}{1 - \frac{\beta}{3}\omega^2 h}\right) \pm \left[\frac{i\omega/h(x/\gamma)}{\sqrt{1 - \omega^2\frac{\beta}{3}h(x/\gamma)}}\right] \times$$

$$\times \sqrt{1 - \frac{\beta}{6\gamma^2}hh'' + \frac{\beta}{3\gamma^2}h'^2 - \frac{h'^2}{\gamma^2}\,\frac{(1-(2/3)\beta\omega^2 h)^2}{h(1-\frac{\beta}{3}\omega^2 h)}}. \tag{3.8}$$

If $h(x/\gamma) \equiv 1$ we recover the usual dispersion relation [46] for the wavenumber ($k = -i\lambda$) in terms of the frequency:

$$k^{\pm}(\omega) = \pm\frac{\omega}{\sqrt{1 - \omega^2\frac{\beta}{3}}}.$$

In practice (i.e., in our experiments) the initial data is generated in space so that the frequencies are bounded by $(3/\beta)^{1/2}$:

$$\omega^{\pm}(k) = \pm\frac{k}{\sqrt{1 + k^2\frac{\beta}{3}}}.$$

On the other hand for the regime of long waves ($\beta \ll 1$) propagating over topographies of decreasing length scales ($\gamma \downarrow$) we observe that

$$\lambda^{\pm}(x) \sim O\left(\frac{1}{\gamma}\right) \pm i\left[\frac{\omega/h(x/\gamma)}{\sqrt{1 - \omega^2\frac{\beta}{3}h(x/\gamma)}}\right] \cdot \sqrt{1 - O\left(\frac{1}{\gamma^2}\right)}. \tag{3.9}$$

The leading order imaginary part plays the role of a local wavenumber, in analogy to the unforced case. Note that as γ tends towards the microscale the spectrum will broaden. But we should bare in mind that this system was not designed to capture rapidly varying topographies. Nevertheless in Figure 3.2 we saw the onset of numerical noise even in the proper regime of validity.

In contrast now consider the linear terrain-following Boussinesq system

$$\begin{aligned} &M(\xi)\eta_t + u_\xi = 0,\\ &u_t + \eta_\xi - \frac{\beta}{3}u_{\xi\xi t} = 0, \end{aligned} \tag{3.10}$$

which was designed for a broad range of topographies [31]. Taking a Fourier transform in time we have that

$$\begin{aligned} &(-i\omega)M(\xi)\hat{\eta} + \hat{u}_\xi = 0,\\ &(-i\omega)\hat{u} + \hat{\eta}_\xi - (-i\omega)\frac{\beta}{3}\hat{u}_{\xi\xi} = 0. \end{aligned} \tag{3.11}$$

By differentiating the first equation and substituting into the second we obtain the following system of ordinary differential equations:

$$\begin{aligned} \hat{u}_\xi &= i\omega \ M(\xi)\ \hat{\eta}, \\ \hat{\eta}_\xi &= \frac{1}{1-\omega^2\frac{\beta}{3}M(\xi)}\left(i\omega\ \ \hat{u} + \omega^2\frac{\beta}{3}M'(\xi)\ \ \hat{\eta}\right). \end{aligned} \tag{3.12}$$

The characteristic polynomial for the variable coeffient matrix of this system is

$$p(\lambda) = \lambda^2 - \lambda\left[\frac{\omega^2\frac{\beta}{3}M'(\xi)}{1-\omega^2\frac{\beta}{3}M(\xi)}\right] + \frac{\omega^2 M(\xi)}{1-\omega^2\frac{\beta}{3}M(\xi)}.$$

The eigenvalues are

$$\lambda^{\pm}(\xi) = \frac{\omega^2\frac{\beta}{3}M'(\xi) \pm i\omega\sqrt{M(\xi)}\sqrt{(1-\omega^2\frac{\beta}{3}M(\xi)) - \beta^2\frac{\omega^2 M'^2(\xi)}{36M(\xi)}}}{2(1-\omega^2\frac{\beta}{3}M(\xi))}. \tag{3.13}$$

If $M(\xi) \equiv 1$ we recover the usual dispersion relation. Recall that the metric term $M(\xi)$ is controlled by two parameters and defined by

$$M(\xi;\beta,\gamma) \equiv 1 + \frac{\pi}{4\sqrt{\beta}} \quad \int_{-\infty}^{\infty} \frac{\delta n(x(\xi_0, -\sqrt{\beta})/\gamma)}{cosh^2\frac{\pi}{2\sqrt{\beta}}(\xi_0-\xi)} d\xi_0 = O(1).$$

Moreover

$$M'(\xi) \equiv \frac{\pi}{2\sqrt{\beta}} \quad \int_{-\infty}^{\infty} \delta n(x(\frac{2\sqrt{\beta}}{\pi}s, -\sqrt{\beta})/\gamma)\frac{senh(s-\tilde{s})}{cosh^3(s-\tilde{s})}ds, \quad \text{where } \ \tilde{s} \equiv \frac{\pi}{2\sqrt{\beta}}\xi.$$

Since $\delta < 1$ and $|n| < 1$, clearly for small β, $|M'|$ scales as

$$|M'(\xi)| \sim \frac{\pi}{\sqrt{\beta}}\int_0^{\infty} \frac{senh(s-\tilde{s})}{cosh^3(s-\tilde{s})}ds = \frac{\pi}{\sqrt{\beta}} \quad \Rightarrow \quad M'(\xi) = O(1/\sqrt{\beta}).$$

Using these results in the dispersion relation (for the eigenvalues) we have that

$$\lambda^{\pm}(\xi) \sim O(\sqrt{\beta}) \pm \ i \ \left[\frac{\omega\ \sqrt{M(\xi;\beta,\gamma)}}{\sqrt{1-\omega^2\frac{\beta}{3}M(\xi;\beta,\gamma)}}\right] \cdot \sqrt{1+O(\beta)}. \tag{3.14}$$

Again the leading order imaginary part plays the role of a local wavenumber, similar to the unforced case. But now the spectrum's range is not sensitive to the microscale as $\gamma \downarrow$. The metric term $M(\xi;\beta,\gamma)$ takes care of it. Moreover, for long waves ($\beta \ll 1$) the spectrum for the multiscale problem remains near the "unforced spectrum". The new mathematical formulation has preconditioned the problem regarding multiscale simulations.

We want to point out that the analysis presented above is not really in favor of the actual solution method for the terrain-following equation. Note that we differentiate $M(\xi)$ in order to obtain the dispersion relation. This is not needed in the solution of the linear equation. A more realistic linear stability analysis corresponds to analyzing the (numerically motivated [45]) setup given through

$$\begin{aligned} \eta_t &= E(\eta, u), \\ V_t &= F(\eta, u), \\ u - \frac{\beta}{3}u_{\xi\xi} &= V \end{aligned} \tag{3.15}$$

where

$$E(\eta,u) = -\frac{1}{M(\xi)}u_\xi,$$
$$F(\eta,u) = -\eta_\xi.$$

This will be described in more detail in the next section. The third equation (3.15) gives rise to a Sturm-Liouville problem due to the usage of an auxiliary function $V(\xi,t)$ in the evolution equations. This is typical in the analysis of KdV-type equations [12] where the solution of (3.15) is given by

$$u(x,t) = \frac{1}{2}\sqrt{\frac{3}{\beta}}\int_{\infty}^{\infty} e^{\sqrt{\frac{3}{\beta}}|x-s|}\; V(s,t)ds.$$

On the other hand for the linear Boussinesq system in cartesian coordinates [45]

$$\begin{aligned} \eta_t &= \tilde{E}(\eta,u),\\ \tilde{V}_t &= F(\eta,u),\\ u - \frac{\beta}{2}(hu)_{xx} + \frac{\beta}{6}h^2u_{xx} &= \tilde{V}, \end{aligned} \tag{3.16}$$

where

$$\tilde{E}(\eta,u) = -(h(x/\gamma)u)_x,$$
$$F(\eta,u) = -\eta_x,$$

and the associated Sturm-Liouville problem from (3.16) is nontrivial, containing rapidly varying disordered coefficients and its derivatives.

We now proceed with the presentation of the numerical scheme for solving the nonlinear terrain-following Boussinesq system in the presence of rapidly varying topographies.

4. Numerical method. The numerical experiments are performed with the nonlinear Boussinesq system (2.1). We use a finite difference Boussinesq solver introduced by Wei and Kirby [45]. This scheme was initially introduced for Nwogu's equations [36] in a slow-varying bottom and we have adapted it for the terrain-following system (2.1) and for equations (3.1). In this section we give details on the implementation of this scheme which works very well for the multiscale problems described.

First we rewrite system (2.1) in a more convenient way, as

$$\begin{aligned} \eta_t &= E(\eta,u),\\ V_t &= F(\eta,u), \end{aligned} \tag{4.1}$$

where

$$\begin{aligned} E(\eta,u) &= -\frac{1}{M(\xi)}\left(\left(1+\frac{\alpha\eta}{M(\xi)}\right)u\right)_\xi,\\ F(\eta,u) &= -\eta_\xi - \frac{\alpha}{2}\left(\frac{u^2}{M(\xi)^2}\right)_\xi, \end{aligned} \tag{4.2}$$

and V is an intermediate variable defined by

$$V = u - \frac{\beta}{3} u_{\xi\xi}.$$

We approximate the solution of system (4.1) by using a high-order predictor-corrector solver. The space-time domain $\xi \in [\xi_1, \xi_J]$, $t \geq 0$ will be discretized by $\xi_j = \xi_1 + (j-1)\Delta\xi,\ 1 \leq j \leq J$ and $t_n = (n-1)\Delta t,\ 1 \leq n \leq N$, respectively. The discretizations of the variables u, η, V will be denoted by u_j^n, η_j^n, V_j^n.

As is well known, predictor-corrector schemes combine two numerical methods. First a third-order explicit Adams-Bashforth solver will be employed to produce a predicted value of (V, η) and then a fourth-order implicit Adams-Moulton scheme is applied to obtain a corrected solution.

The **explicit predictor** step is given by

$$\begin{aligned} \eta_j^{n+1} &= \eta_j^n + \frac{\Delta t}{12}(23E_j^n - 16E_j^{n-1} + 5E_j^{n-2}), \\ V_j^{n+1} &= V_j^n + \frac{\Delta t}{12}(23F_j^n - 16F_j^{n-1} + 5F_j^{n-2}), \end{aligned} \tag{4.3}$$

where the values at levels $n-2,\ n-1,\ n$ are known. Furthermore the notation $E_j^n = E(\eta_j^n, u_j^n)$ and $F_j^n = F(\eta_j^n, u_j^n)$ is used. In this step some remarks should be made. The first-order derivatives in ξ in equations (4.2) are approximated to fourth-order accuracy. Computation of η_j^{n+1}, V_j^{n+1} from equations (4.3) is straightforward. Nevertheless, in evaluating the fluid velocity u_j^{n+1} we must solve the (spatial) ordinary differential equation

$$u - \frac{\beta}{3} u_{\xi\xi} = V, \tag{4.4}$$

which is forced by the known left handside V_j^{n+1}. Equation (4.4) is discretized by the second-order approximation

$$u_j^{n+1} - \frac{\beta}{3}\left(\frac{u_{j+1}^{n+1} - 2u_j^{n+1} + u_{j-1}^{n+1}}{\Delta\xi^2}\right) = V_j^{n+1},$$

for $2 \leq j \leq J-1$. To evaluate the boundary values u_1^{n+1} and u_J^{n+1}, we use the linear radiation conditions (Engquist and Majda [14]):

$$\begin{aligned} u_t - u_\xi = 0, &\quad \text{at } \ \xi = \xi_1, \\ u_t + u_\xi = 0, &\quad \text{at } \ \xi = \xi_J, \end{aligned} \tag{4.5}$$

where ξ_1 and ξ_J denote the left and right ends of the computational domain. The conditions above play the role of absorbing the waves arriving at the boundaries of the computational domain. Thus, to go back from variable V to u, only a **tridiagonal linear system** of dimension $J-2 \text{ x } J-2$ must be solved. We remark that this system's matrix is constant in time and just one LU decomposition must be performed at the starting point. This decomposition may be stored to be used at each time step.

Once the predicted values η_j^{n+1}, u_j^{n+1} are obtained we compute E_j^{n+1}, F_j^{n+1} from equations (4.2). The **corrected values** are calculated from

$$\eta_j^{n+1} = \eta_j^n + \frac{\Delta t}{24}(9E_j^{n+1} + 19E_j^n - 5E_j^{n-1} + E_j^{n-2}),$$
$$V_j^{n+1} = V_j^n + \frac{\Delta t}{24}(9F_j^{n+1} + 19F_j^n - 5F_j^{n-1} + F_j^{n-2}), \tag{4.6}$$

where the quantities at level $n+1$ are computed iteratively by using the predicted approximation as initial value. The new u_j^{n+1} is computed from V_j^{n+1} as in the predictor step. We stop the iteration process when the relative error between two sucessive corrected values η^{n+1}, u^{n+1} and $\eta^{(n+1)^*}$, $u^{(n+1)^*}$ satisfy

$$\Delta u^{n+1} = \frac{\sum_i \left| u_j^{n+1} - u_j^{(n+1)^*} \right|}{\sum_i \left| u_j^{n+1} \right|} < tol \qquad \text{and} \qquad \Delta \eta^{n+1} = \frac{\sum_i \left| \eta_j^{n+1} - \eta_j^{(n+1)^*} \right|}{\sum_i \left| \eta_j^{n+1} \right|} < tol.$$

We set $tol = 0.001$. This tolerance is achieved with only one iteration in all our experiments.

The numerical scheme described above can be adapted for the model (3.1). The main difference is in solution of the linear tridiagonal system required to interchange from the intermediate variable V to the physical velocity u. In contrast to the terrain-following system (2.1), in formulation (3.1) the corresponding system's matrix depends on the the physical depth $h(x)$ and its derivatives $h'(x)$, $h''(x)$. The effect of this fact in the Boussinesq solver was discussed in the preceding section.

The computational cost of the scheme is found to be linear. Moreover it is formally second-order accurate in space and fourth-order accurate in time [29]. The above mentioned features make this scheme very accurate and cheap. In [30] we used it in the validation of the O'Doherty-Anstey theory for dispersive waves in the presence of highly-disordered orographies. It was found to capture very well the cumulative effect of the fine details of the orography and to model the dispersive properties of system (2.1). In particular, we showed the excellent agreement between the computational experiments and the linear theoretical results for the apparent diffusion of pulses due to orographic forcing. The scheme captured extremely well both the (smooth) coherent wavefront as well as the (highly oscillatory) incoherent signal. Details and properties of the numerical scheme were not discussed in [30].

In the above sections we have presented the numerical impact of the new terrain-following formulation together with details of the numerical scheme considered. In the following sections we present numerical results that are beyond the scope of the theory presented in [30]. Of particular interest are the experiments with solitary waves. In a scientific computing spirit we hope to provide insight for the development of new mathematical theory in these topics, in particular for the O'Doherty-Anstey (ODA) theory and time-reversal of solitary waves. Recently progress has been made for weakly nonlinear waves [21]. Fouque, Garnier and Nachbin showed that the apparent diffusion due to the random medium regularizes the shock. This allows for time-reversal in transmission experiments beyond the shock formation distance.

5. Pulse-shape stabilization. In this section we use the Boussinesq solver described in the previous section to explore the effect of **stabilization** in weakly-nonlinear, weakly-dispersive waves (in particular solitary waves) in the presence of highly-disordered orographies. We find that the transmitted coherent front (i.e. the smooth leading part of the signal) stabilizes to a deterministic shape which is independent of the particular medium realization when observed relative to its corresponding first arrival time (travel time) up to a fixed observation station into the medium. This phenomenon is observed at large distances from the disturbance's source and is of great interest because in a real situation the detailed properties of a particular propagation medium are not exactly known.

The stabilization property in disordered media has been studied for hyperbolic models in one dimension in [26] and extended to multiple dimensions in [27] by using probabilistic techniques. This is an aspect that makes the O'Doherty-Anstey theory very robust. Namely, we have that the pulse shaping, due to the apparent diffusion mechanism, is deterministic depending only on statistics of the disordered forcing. Stabilization is usually proved through stochastic modeling by showing that the variance of the pulse shaping process tends to zero in the appropriate limit [39]. Recently the results of [30] lead to a probabilistic ODA theory for linear dispersive waves [20]. Here we give strong evidence of stablization (which has never been proved) for weakly-dispersive, weakly-nonlinear waves.

In the numerical simulations, as was done in [30], the free surface coefficient $M(\xi)$ in system (2.1) is synthetized as

$$M(\xi) = 1 + \delta n(\xi/\gamma), \tag{5.1}$$

where $n(\xi)$ is a mean-zero piecewise linear function, constructed by using a random number generator in the interval [-1,1], $0 < \delta < 1$ is the amplitude of fluctuations.

Two types of initial disturbances are considered. First, Gaussian-shaped disturbances

$$u(\xi, 0) = \eta(\xi, 0) = e^{-(\xi-\xi_o)^2/\epsilon}, \tag{5.2}$$

where the parameter ξ_o controls the pulse's initial position and $\epsilon > 0$ its effective width. Also, solitary waves of the form

$$\begin{aligned} \eta(\xi, 0) &= A_1 \ \mathrm{sech}^2(B(\xi - \xi_o)) + A_2 \ \mathrm{sech}^4(B(\xi - \xi_o)), \\ u(\xi, 0) &= A \ \mathrm{sech}^2(B(\xi - \xi_o)), \end{aligned} \tag{5.3}$$

where

$$A_1 = \frac{C^2 - 1}{\alpha C^2} = \frac{1}{C^2}, \quad C = \sqrt{1+\alpha}, \quad A_2 = \frac{(C^2-1)^2}{\alpha C^2} = \frac{\alpha}{C^2}, \tag{5.4}$$

and

$$A = \frac{C^2 - 1}{\alpha C} = \frac{1}{C}, \quad B = \left\{ \frac{C^2 - 1}{(4/3)\beta C^2} \right\}^{1/2} = \left\{ \frac{\alpha}{(4/3)\beta C^2} \right\}^{1/2}. \tag{5.5}$$

Note that $A_1 + A_2 = 1$ and that all the constants involved are determined by the values of the parameters α and β. Equations (5.3) are approximate travelling wave solutions for the nonlinear Boussinesq system (2.1). See Wei and Kirby [45] for details.

In Figure 5.1(a) we plot the solution of system (2.1) for a constant depth channel with $\alpha = 0.001$ and $\beta = 0.005$. In this case, the oscillatory coda following the pulse is deterministic and is only due to the models dispersion. Furthermore, (when $\alpha = \beta$) a solitary wave solution in the form of (5.3) propagates without changing its shape (c.f. Figure 5.1(b)). The pulse does not develop a coda due to the balance between the nonlinear and dispersive effects.

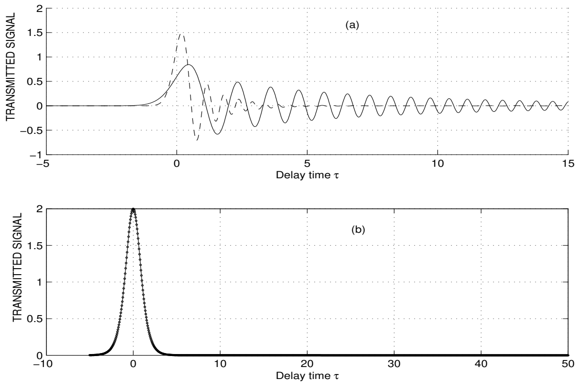

FIG. 5.1. *(a) In dashed line : Initial disturbance. Solid line : Solution in a constant depth at* $\xi = 40$*. Parameters:* $\alpha = 0.001$*,* $\beta = 0.005$*. (b) Solitary wave in a constant depth for* $\alpha = \beta = 0.002$*. In solid line : solitary wave at* $\xi = 0$*. In dotted line : solitary wave at* $\xi = 150$ *(25 pulse widths). Notice that the shape of the solitary wave does not change as it propagates in contrast to the pulse in (a).*

The first stabilization case we illustrate uses $\alpha = 0.001$ and $\beta = 0.0005$ which effectively is not dispersive. We start with small parameters in order to contrast with other regimes. Ten different realizations of the synthetic disordered orographies (defined as in (5.1)) are considered in this experiment. In all of them the amplitude of the fluctuation is $\delta = 0.5$, the correlation length is $\ell = 0.1$ and the fluctuations are located over the interval [0,45]. The realizations all have the same statisitics. A rightgoing Gaussian located at $\xi_o = -5$ propagates over each orography and is recorded in time at the same medium station $\xi = 40$. In Figure 5.2 we superimpose the traces of the resulting transmitted pulses plotted as a function of the pulse's delay time $\tau = t - x$. Here x is the travel time given by

$$x = \int_0^{\xi} \frac{1}{C_o(s)} ds, \tag{5.6}$$

with $C_o(s) = M(s)^{-1/2}$. Observe that the shape of the wave's coherent front (approximately within the time interval $[-1, 1]$) varies very little (stabilizes) from one realization to another. This part of the transmitted signal resembles the incoming Gaussian perturbation with smaller amplitude due to apparent diffusion. This O'Doherty-Anstey attenuation is the result of the cumulative effect regarding the multiple scattering which takes place within the disordered medium. In contrast, the pulse's incoherent coda depends highly on the particular realization of the orography.

We remark that the pulse only stabilizes when it is observed in the random travel time frame [39]. Figure 5.3 corroborates with this. We graph the same pulses as in Figure 5.2 but now as a function of the clock time t. Note that the time of arrival of each pulse at the fixed medium station fluctuates around $t = 40$ and the stabilization does not take place. Pulse shape stabilization in the hyperbolic regime has been observed numerically elsewhere [34, 42]. In this work, we extend these stabilization experiments to dispersive waves, which was proved but not shown in [20].

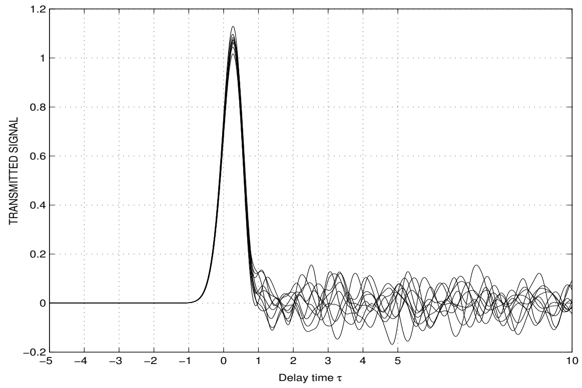

FIG. 5.2. *Transmitted pulse shape stabilization observed at the fixed medium's station* $\xi = 40$ *(40 pulse widths). This plot is obtained by propagating a Gaussian pulse over ten different realizations of synthetic orographies. Each trace corresponds to a realization. The parameters are* $\alpha = 0.001$ *and* $\beta = 0.0005$.

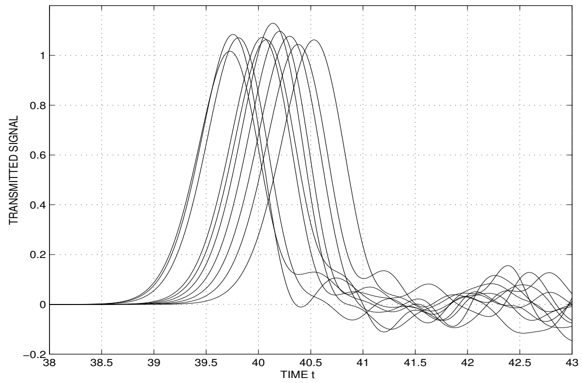

FIG. 5.3. *The same as in Figure 5.2 but now the pulses are graphed in the clock time* t. *The stabilization is not observable in this frame.*

Next we repeat the experiment above by increasing the dispersion parameter ten times ($\beta = 0.005$). This is a nonegligible level of dispersion due to the long propagation distance (macroscale) considered. Other parameters are left unchanged. The results are presented in Figure 5.4. Again we have the stabilization of the coherent signal within the time interval $[-5, 2]$. In the interval [2,5] stabilization is being lost. The oscillatory segment of the wave within this interval is due to model's effective dispersion, modified by the presence of randomness [20]. Compare it to the effectively hyperbolic regime in Figure 5.2. Beyond $\tau = 5$ we find the incoherent codas. We point out that the disordered codas appear due to the interaction between the wave and the particular disordered medium and they do not stabilize. It is well known [8, 7] that stabilization is connected with the pulse being broadband. Since the dispersive coda is essentially monocromatic [46], it is not as statistically stable as the front (it will be partially affected by the particular realization of the medium).

Finally we consider the case of rightgoing solitary waves of the form (5.3). The levels of nonlinearity and dispersion are increased to $\alpha = \beta = 0.01$. In all eight orographies considered the fluctuations are located over the interval [0,120], their amplitude is $\delta = 0.5$ and their correlation length is taken to be $\ell = 0.6$. The effective width of the solitary wave is about 6 units so that we want to keep the 1/10 ratio as for the Gaussian. In Figure 5.5 we plot the transmitted pulses recorded at a distance 120 units to the right side of the origin (corresponding to 20 pulse widths). The stabilization is observed along the front within the time interval of approximately $[-5, 3]$

Pulse shaping stabilization is a very robust phenomenon connected with waves in disordered (random) media. The O'Doherty-Anstey theory is well understood for hyperbolic [6, 39] and linear dispersive waves [20, 29, 30]. Some recent results were obtained for weakly-nonlinear hyperbolic waves [21]. But there is still a lack of mathematical theory (both the O'Doherty-Anstey effect and stabilization) for solitary waves. As mentioned above the scientific computing spirit of these experiments is to shed some light in this direction.

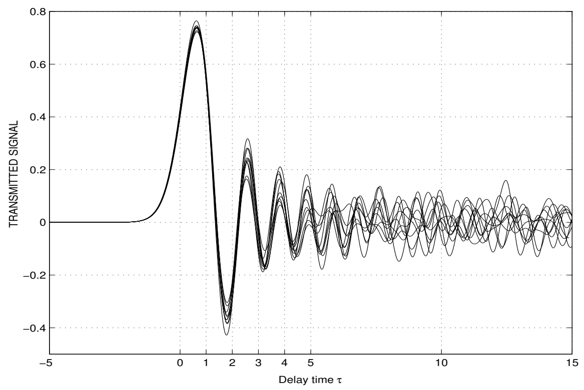

FIG. 5.4. *Pulse shape stabilization for a higher dispersion level at $\beta = 0.005$. Other parameters are equal to those indicated in Figure 5.2.*

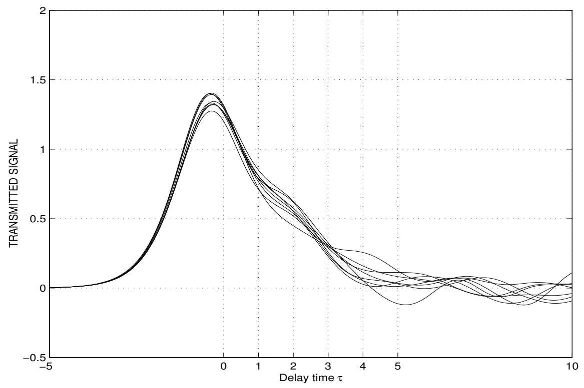

FIG. 5.5. *Transmitted pulse shape stabilization observed at the fixed medium's station $\xi =$ 120 (20 pulse widths). This plot is obtained by propagating a solitary wave over eight different realizations of synthetic orographies. The parameters are $\alpha = \beta = 0.01$.*

6. Time-reversal and refocusing. When a pulse travels through a long highly disordered medium its shape is strongly modified and multiple reflections arise as was shown above. An amazing fact is that the reflected signal produced by this wave-orography interaction can be used to **refocus** (recover) the initial disturbance. As mentioned in the Introduction this property of a highly disordered medium was extensively analyzed by Fink [17] in the context of linear acoustic waves. Moreover most experiments were done for time-reversal in transmission (**TRT**). In [19] results for the time-reversal in reflection (**TRR**) were presented for hyperbolic water waves (shallow water waves). Many other applications were described in the Introduction. Here solitary waves are considered in detailed experiments for the first time.

In this section we wish to explore refocusing for weakly-nonlinear, weakly-dispersive waves modeled by the terrain-following Boussinesq system (2.1). We start by considering **time reversal in reflection** which was first proved, for hyperbolic problems in random media, by Clouet and Fouque [9].

6.1. Time-reversal in reflection (TRR). We start with several numerical illustrations of the TRR refocusing phenomenon. The orography fluctuations cover the interval [5,45] and its amplitude is $\delta = 0.5$. The parameters for the numerical solver are $J = 12000$, $N = 14000$, $\Delta\xi = 0.0075$ and $\Delta t = 0.0036$ and the computational domain is [-40,50]. It is sufficiently large to enable us to record a long part of the reflected signal emerging from the medium.

The setup employed to produce the pulse refocusing is explained in Figure 6.1 for the wave elevation field. We set $\alpha = 0.001$ and $\beta = 0.002$. A Gaussian disturbance $\eta(\xi, 0) = u(\xi, 0) = h(\xi)$ (see Figure 6.1(A)) is located at the left of the origin, say $\xi_o = -5$, and allowed to propagate to the right. At time $t = t_1$ ($t_1 = 50$) we record the reflected wave elevation $\eta(\xi, t_1)$ and the velocity $u(\xi, t_1)$ and cut part of them at the left of the origin. A possible choice is the window within the dashed lines indicated in (B). Here we use $G = 1_{[\ell_0, 0]}$ (the indicator function of the interval $[\ell_0, 0]$) as the cutoff function as in the notation adopted in [9, 20]. In this experiment we set $\ell_0 = -40$.

Now the time-reversal method (in reflection) consists in changing the sign of the velocity field so that the signal $\eta_o(\xi) = \eta(\xi, t_1)G(\xi)$, $u_o(\xi) = -u(\xi, t_1)G(\xi)$ corresponds to a "new" rightgoing initial data which is sent back into the **same medium** (see (C)) in its reverse time of arrival: last information in, first information out. This incoherent data propagates into the random medium and recompresses into a smooth coherent profile. In (D) we see a "clean" refocused pulse similar to $h(\xi)$ arising at its original location $\xi_o = -5$ exactly at time $t_1 = 50$. Thus a "small copy" of the incoming pulse has been recompressed from the incoherent reflected signal as predicted in [9] and fully illustrated in [19] for hyperbolic waves. We remark that if at this step the medium is replaced by a different realization of the orography refocusing **never** takes place. But if only a small random perturbation is added to the random medium, recompression is still observed [1] and can be quantified. In this case recompression is obviously less efficient than in the unperturbed case. In the present work dispersive refocusing for TRR is done for the first time. At the same time Fouque, Garnier and Nachbin [20] obtained a complete probabilistic theory for the time reversal of linear dispersive waves and presented refocusing results for TRT.

We now increase the dispersion parameter to $\beta = 0.01$. The other parameters are the same as in the preceding experiment. The resulting refocused pulse is graphed in Figure 6.2 where it is superimposed to the refocused pulse for $\beta = 0.002$. A remarkable fact is that the model's dispersion does not affect the shape of the TRR refocused pulse even at larger values of dispersion. This is explained in [20] through the full recompression of the Airy-like coda, namely the complete reversibility of the dispersive process even in a homogeneous medium. For the case $\beta = 0.01$ we examine in Figure

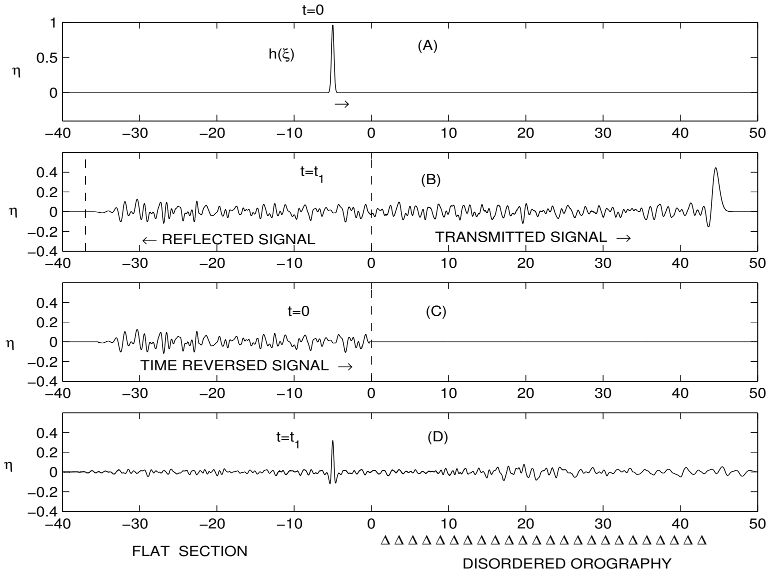

FIG. 6.1. *The time reversal setup. In (A) we visualize the initial disturbance. In (B) the signal after travelling a distance of 50 units of channel ($t = t_1$). In (C) we indicate with dashed lines the signal's section considered for the time-reversal method. This "new" signal is sent back into the medium. In (D) the refocused pulse arises exactly at time $t = t_1$. Parameters :* $\alpha = 0.001$, $\beta = 0.002$.

6.3 the wave elevation at several time stages before its (final) refocusing (i.e., full recompression) . A left propagating Airy-like pulse is observed in (A). The dispersive oscillation (now) ahead of the wave progressively recompresses as time approaches $t = 50$, the exact instant in which refocusing takes place. At this time we observe a relatively "clean" pulse (see (E)) where the dispersive effects have disapeared. Thus the dispersive tail has been fully recompressed. This is a remarkable phenomenon only observable when dispersion is present: the incoherent signal recompressed into an oscillatory wave that further recompressed into a pulse. Mathematically this is expressed in [20] by the composition of two different types of convolutions: a diffusive (with a Gaussian kernel) and a dispersive (with an Airy kernel).

6.2. Refocusing of a solitary wave for TRR and TRT. The previous numerical experiments illustrated the TRR refocusing of waves in effectively linear, weakly-dispersive regime. Now we examine the refocusing property with solitary waves for which no theory is available. This is an interesting experiment because weak nonlinearity is introduced to balance dispersion ($\alpha = \beta = 0.01$). The orography's fluctuations cover the interval [0,120], its amplitude is $\delta = 0.5$ and its correlation length is taken to be $\ell = 0.6$ and we still have $\gamma \approx 0.1$. The numerical parameters are $J = 13000$, $N = 10000$, $\Delta\xi = 0.027$ and $\Delta t = 0.015$ and the computational domain is [-200,150]. The setup for the time-reversal of solitary waves can be seen in Figure 6.4. The TRR refocused pulse and the initial solitary wave (in the form of (5.3)) are graphed in Figure 6.5. The incoherent reflected signal has been time-reversed, propagated over a distance of 20 pulse widths (approximately 120 units of length), has recompressed and finally we recover approximately 20% of the original incoming energy. The majority of the energy has been transmitted (c.f. Figure 6.4).

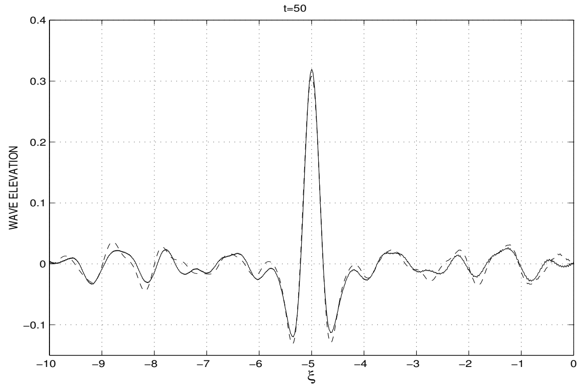

FIG. 6.2. *Refocusing of a Gaussian pulse for two levels of dispersion:* $\beta = 0.002$ *(in solid line) and* $\beta = 0.01$ *(in dashed line).*

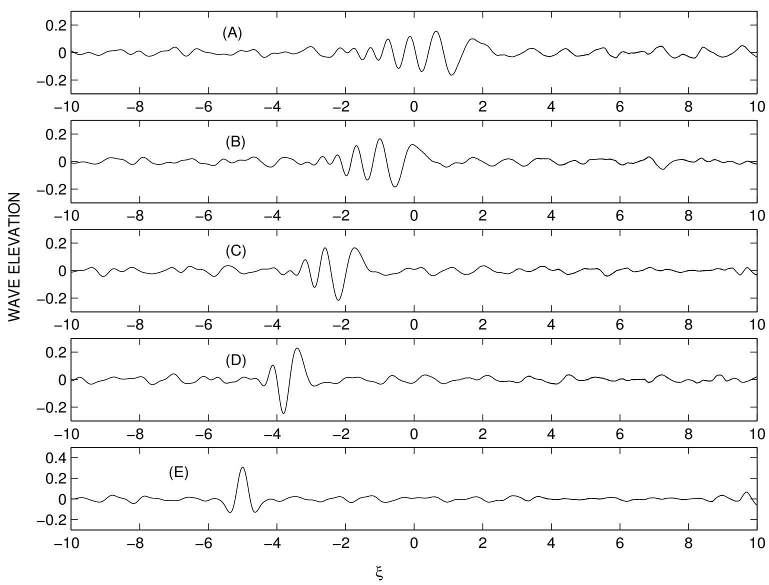

FIG. 6.3. *Dispersive refocusing mechanism. From top to bottom the plots correspond to the wave elevation at times* $t = 43.2, 44.6, 46.4, 48.2, 50$*, respectively. Parameters :* $\alpha = 0.001$ *and* $\beta = 0.01$.

Note that a solitary wave, being a robust coherent structure, sheds less reflection than for example a weakly nonlinear hyperbolic wave [21]. Hence there is less energy to recompress under TRR. On the other hand, as mentioned above, when we perform TRT the refocused pulse has a larger amplitude as seen in Figure 6.6.

In Figure 6.7 we can see several snapshots of the time-reversed propagation for the transmitted wave. Note that some of the leading incoherent energy is being recompressed into the smooth wavefront, but apparently at a slower rate than in the linear regime. Moreover (apparently) there is more reflection in the time-reversed experiment than was noted for the weakly nonlinear study [21]. Another interesting fact is that the pulse that emerges on the homogeneous left side of the channel is a travelling wave. In Figure 6.8 we centered the last 3 snapshots, each 3.75 time units

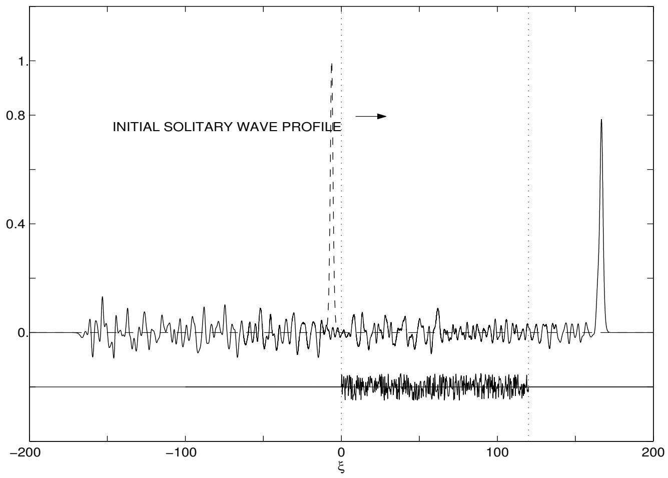

FIG. 6.4. *Setup for the time-reversal of solitary waves. TRR uses the reflected signal at the left and TRT the transmitted pulse together with the incoherent signal to the right.*

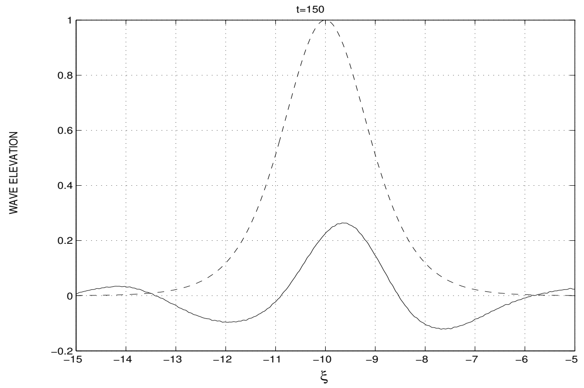

FIG. 6.5. *In dashed line : initial solitary wave. In solid line : TRR refocused solitary wave. The parameters are* $\alpha = \beta = 0.01$.

appart, and we clearly see that the wave profile is unchanged.

There are no doubts that all these facts here discussed for solitary waves need a further mathematical study and we hope that these scientific computing experiments with solitary waves has shed some light in this direction.

6.2.1. Stabilization in time-reversal. For one dimensional hyperbolic waves Clouet and Fouque [9] show that the shape of the refocused pulse does not depend on the particular medium's realization considered. They call it **the refocusing self-averaging property**. Further studies on the refocusing and self-averaging of linear waves are [4, 5, 20, 22]. Here we explore it in the context of weakly-nonlinear, weakly-dispersive waves. Our intention is to give numerical evidence of the phenomenon hoping that it will help in the development of new mathematical theory.

Consider a solitary wave located at $\xi_o = -10$. The nonlinearity and dispersion parameters are set to $\alpha = \beta = 0.01$. Again the fluctuations of the orography cover the interval [0,120], their amplitude is $\delta = 0.5$ and the correlation length is $\ell = 0.6$.

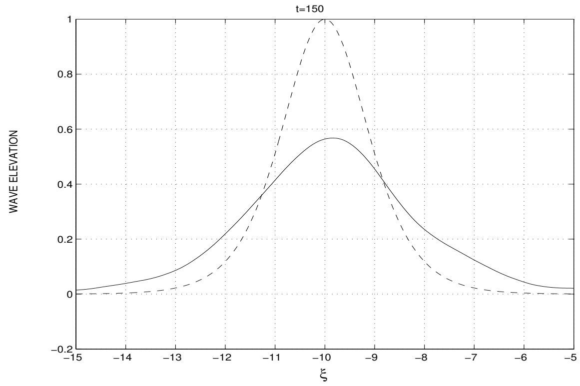

FIG. 6.6. *In dashed line : initial solitary wave. In solid line : TRT refocused solitary wave. The parameters are* $\alpha = \beta = 0.01$.

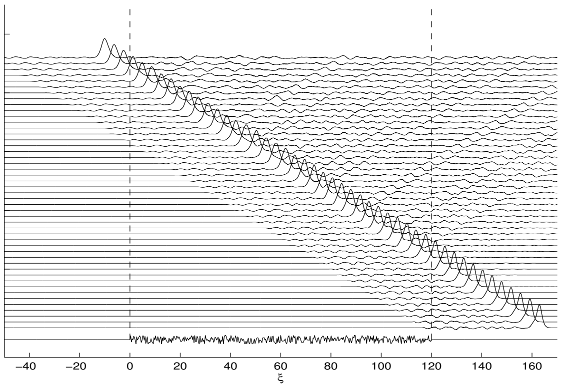

FIG. 6.7. *Snapshots for the TRT of the solitary wave evolving upwards at increments of 3.75 time units. The bottom trace represents the topography together with the initial time-reversed wave elevation.*

The cutoff time for the time-reversal method is $t_1 = 150$ in all cases. The TRR results for eight different realizations of the medium are presented in Figure 6.9. The stabilization of the shape of the refocused pulse takes place within the interval [-12,-8] where the maximun difference between the traces is small. Furthermore about 25% to 30% ("amplitude-wise") of the incoming solitary wave is refocused in these eight experiments. The linear theory for stabilization predicts that the refocused profile is deterministic in the limit as $\ell = \varepsilon \downarrow 0$. Here, of course, ε is small but finite and we see a small fluctuation in the final amplitude. But we clearly see that the fluctuations about the smooth refocused profile are much larger. In Figure 6.10 we have the stabilization in transmission. The refocused shape is again effectively deterministic.

7. Conclusions. The first contribution of this paper was to show, through a linear stability analysis, how changing from a cartesian to a curvilinear coordinate system the eigenvalues of the underlying problem are completely rescaled and the problem better conditioned for multiscale simulations. The change of coordinates removed the stiffness, promoted by the microscale forcing, in the sense that the spatially dependent eigenvalues (of the forced problem) lie (nearly) in the same range as those

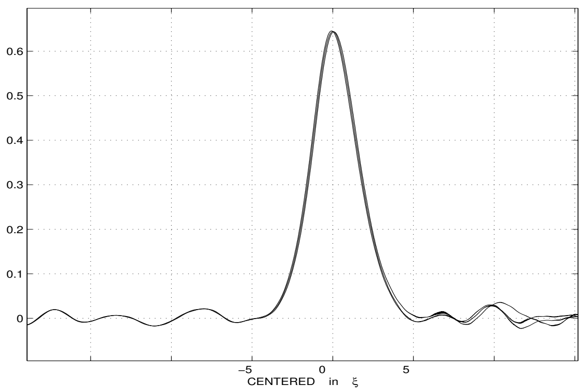

FIG. 6.8. *The last 3 snapshots of Figure 6.7 were centered. The left propagating wave profile is unchanged.*

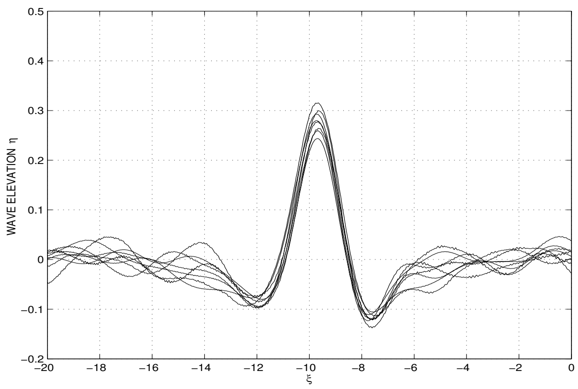

FIG. 6.9. *TRR refocusing stabilization for a solitary wave over eight different synthetic orography realizations. The model parameters are* $\alpha = \beta = 0.01$.

for the unperturbed problem. This was not the case when the problem was formulated in cartesian coordinates since the eigenvalue range scaled like the reciprocal of the microscale.

Our second contribution was to perform *scientific computing simulations* with our stable Boussinesq solver in the presence of *multiple scales*: the topographic *microscale*, the wave's *mesoscale* for long propagation distances (*macroscale*). The major goal of these simulations was the time-reversal of solitary waves. Recently time-reversal results were obtained for linear weakly dispersive waves [20] and for weakly nonlinear waves [21]. Both studies made use of the asymptotic analysis of stochastic differential equations. At this time there is no theory for both ingredients combined. In the near future we hope to extend this technology, of the papers mentioned above, to weakly dispersive, weakly nonlinear waves, in particular to solitons.

REFERENCES

[1] D.G. Alfaro Vigo, J.P. Fouque, J. Garnier and A. Nachbin, Robustness of time reversal for waves in time-dependent random media, submitted for publication (2003).

[2] M. Ash, W. Kohler, G. Papanicolaou, M. Postel and B. White. *Frequency content of*

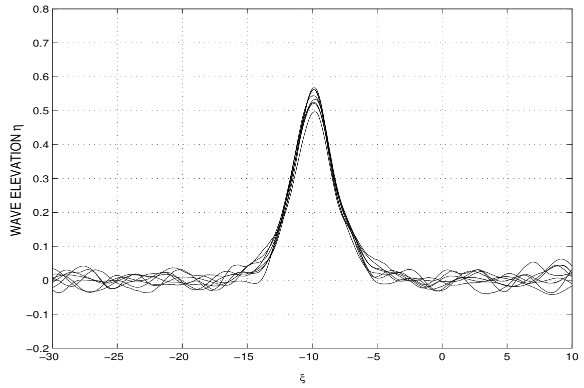

FIG. 6.10. *TRT refocusing stabilization for a solitary wave over eight different synthetic orography realizations. The model parameters are* $\alpha = \beta = 0.01$.

randomly scattered signals, SIAM Review 33 (1991), pp. 519-625.

[3] P.G. BAINES, *Topographic Effects in Stratified Flows*, Cambridge Univ. Press, 1995.

[4] G. BAL, G. PAPANICOLAOU AND L. RYZHIK, *Self-averaging in time reversal for the parabolic wave equation*, Stochastics and Dynamics, **2**, (2002) 507-532.

[5] P. BLOMGREN, G. PAPANICOLAOU, AND H. ZHAO, *Super-Resolution in Time-Reversal Acoustics*, JASA, **Vol. 111**, (2002), pp. 230-248.

[6] L. BERLYAND, L. AND R. BURRIDGE. *The accuracy of the O'Doherty-Anstey approximation for wave propagating in highly disordered stratified media*, Wave Motion 21 (1995), pp. 357-373.

[7] R. BURRIDGE, G. PAPANICOLAOU AND B.S. WHITE. *One-dimensional wave propagation in a highly discontinuous medium*, Wave Motion 10 (1988), pp. 19-44.

[8] R. BURRIDGE, G. PAPANICOLAOU, P. SHENG AND B. WHITE, *Probing a random medium with a pulse*, SIAM J. Appl. Math., Vol. 49, No. 2, (1989) pp. 582-607.

[9] J.F. CLOUET AND J.P. FOUQUE. *A time-reversal method for an acoustical pulse propagating in randomly layered media*, Wave Motion (1997), 25, pp. 361-368.

[10] A. DERODE, P. ROUX AND M. FINK, *Robust acoustic time reversal with high-order multiple scattering*, Phys. Rev. Lett., **vol. 75**, No. 23, (1995) pp.4206-4209.

[11] A. DERODE, A. TOURIN AND M. FINK, *Random multiple scattering of ultrasound. II: Is time reversal a self-averaging process?*, Phys. Rev. E, **64**, No. 3, (2001) p. 6606.

[12] P.G. DRAZIN AND R.S. JOHNSON, *Solitons: an introduction*, Cambridge University Press, (1989).

[13] T. DRISCOLL. http://www.math.udel.edu/driscoll/software.

[14] B. ENGQUIST AND A. MAJDA. *Absorbing boundary conditions for the numerical simulation of waves*, Math. Comp. 31 (139), (1977), pp. 629-651.

[15] EUROPEAN CENTRE FOR MEDIUM-RANGE WEATHER FORECASTS (ECMWF), *Orography*, Proceedings of a Workshop held at ECMWF, (1998).

[16] M. Fink *Time reversal mirrors*, J. Phys. D: Appl. Phys., **26**, (1993) pp. 1333-1350.

[17] M. FINK. *Time-reversed acoustics*, Scientific American (1999), pp. 67-93.

[18] M. FINK AND C. PRADA, *Eigenmodes of the time reversal operator: a solution to selective focusing in multiple-target media*, Wave Motion, **20**, (1994) pp. 151-163.

[19] J.P. FOUQUE AND A. NACHBIN. *Time-reversed refocusing of surface water waves*, SIAM Multiscale Modeling and Simulation, Vol.1, No.4, (2003), pp. 609-629.

[20] J.P. FOUQUE, J. GARNIER AND A. NACHBIN. *Time reversal for dispersive waves in random media*, accept for publication, SIAM J. Appl. Math., (2003).

[21] J.P. FOUQUE, J. GARNIER AND A. NACHBIN, Shock structure due to stochastic forcing and the time reversal of nonlinear waves, submitted for publication (2003).

[22] J.P. FOUQUE AND K. SØLNA, Beating the diffraction limit in laminated media, SIAM Journal on Multiscale Modeling and Simulation Vol. 1. No. 2, (2003) pp. 239-259.

[23] T. Y. HOU, J. LOWENGRUB AND M. SHELLEY, Removing the Stiffness from Interfacial Flows with Surface Tension , J. Comput Phys. , 114 (1994), pp. 312-338.

[24] J.S. KIM, H.C. SONG AND W.A. KUPERMAN, *Adaptive time-reversal mirror*, J. Acoust. Soc. Am., **109**, 1817-1825, (2001).

[25] W.A. Kuperman, W.S. Hodgkiss, H.C. Song, T. Akal, C. Ferla andD.R. Jackson, *Phase conjugation in the ocean: Experimental demonstration of an acoustic time reversal mirror*, J. Acoust. Soc. Am., **103**, 25-40, (1998).
[26] P. Lewicki, R. Burridge and G. Papanicolaou. *Pulse stabilization in a strongly heterogeneous layered medium*, Wave Motion 20 (1994), pp. 177-195.
[27] P. Lewicki, R. Burridge and M. de Hoop. *Beyond effective medium theory: Pulse stabilization for multimode wave propagation in high-contrast layered media*, SIAM J. Appl. Math. 56, No. 1 (1996), pp. 256-276.
[28] C.C. Mei. *The applied dynamics of ocean surface waves*, John Wiley, 1983.
[29] J.C. Muñoz Grajales. *Dispersive wave attenuation and refocusing due to disordered orographic forcing*. PhD. dissertation, IMPA, 2002.
[30] J.C. Muñoz Grajales and A. Nachbin. *Dispersive wave attenuation due to orographic forcing*, accepted for publication, SIAM J. Appl. Math., (2003).
[31] A. Nachbin. *A terrain-following Boussinesq system*, SIAM J. Appl. Math., vol. 63, No. 3 (2003), pp. 905-922.
[32] A. Nachbin, *The localization length of randomly scattered water waves,* J. Fluid Mech., **vol. 296**, (1995) 353-372.
[33] A. Nachbin and V. Casulli, *Water waves: linear potential theory results validated with a hydrostatic Navier-Stokes model,* In: Mathematical and Numerical Aspects of Wave Propagation, Editor J. A. DeSanto, SIAM, (1998).
[34] A. Nachbin and K. Sølna, *Apparent diffusion due to topographic microstructure in shallow waters,* Phys. Fluids, **vol. 15**, No. 1, (2003) 66-77.
[35] J. Ndzie, *Refocusing of a time-reversed acoustical pulse propagating in randomly layered media*, J. Stat. Phys., **Vol. 104**, No. 516, (2001).
[36] O. Nwogu, O. *Alternative form of Boussinesq equations for nearshore wave propagation*, J. Waterway, Port, Coastal and Ocean Engineering, 119 (1993), pp. 618-638.
[37] C. Pires and M.A. Miranda, *Tsunami waveform inversion by adjoint methods*, J. Geophys. Res., **vol. 106**, No. C9 (2001), pp. 19733–19796.
[38] G. Papanicolaou, L. Ryzhik and K. Sølna, *Statistical stability in time reversal*, to appear in SIAM Journal of Applied Mathematics, 2003.
[39] G. Papanicolaou and K. Sølna. *Ray theory for a locally layered random medium*, Waves in Random Media 10 (2000), pp. 151.
[40] D.H. Peregrine. *Long waves on a beach*, J. Fluid Mech. 27 (1967), pp. 815-827.
[41] C. Prada and M. Fink. *Eigenmodes of the time reversal operator : A solution to selective focusing in multiple-target media*, Wave Motion 20 (1994), pp. 151-163.
[42] K. Sølna. *Stable spreading of acoustic pulses due to laminated microestructure*. Ph.D. dissertation, Stanford University, 1997.
[43] K. Sølna, Focusing of time-reversed reflections, Waves Random Media (2002), **12**, pp. 365-385.
[44] M. Tanter, J.L. Thomas, F. Coulouvrat and M. Fink,*Breaking of time reversal invariance in nonlinear acoustics,* Phys. Rev. E, **vol. 64**, No. 1, (2001) p 6602.
[45] G. Wei and J. Kirby. *Time-dependent numerical code for extended Boussinesq equations*, J. of Waterway, Port, Coastal and Ocean Engineering, vol. 121, No. 5 (1995), pp. 251-261.
[46] G.B. Whitham *Linear and nonlinear waves*, John Wiley, (1974).